SOLID-PROPELLANT GENERAL DEFORMATIONS AND THEIR EFFECTS ON MOTOR PERFORMANCE

David Franklin Smith

Certificate of Approval

John E. Burkhalter
Assistant Professor
Aerospace Engineering

Richard H. Sforzini, Chairman
Professor
Aerospace Engineering

Malcolm A. Cutchins
Associate Professor
Aerospace Engineering

Winfred A. Foster, Jr.
Assistant Professor
Aerospace Engineering

SECURITY CLASSIFICATION OF THIS PAGE (When Data Entered)

REPORT DOCUMENTATION PAGE	READ INSTRUCTIONS BEFORE COMPLETING FORM
1. REPORT NUMBER: CI 79-4	2. GOVT ACCESSION NO. / 3. RECIPIENT'S CATALOG NUMBER
4. TITLE (and Subtitle): Solid Propellant General Deformation and the Effects on Motor Performance	5. TYPE OF REPORT & PERIOD COVERED: Thesis
	6. PERFORMING ORG. REPORT NUMBER
7. AUTHOR(s): Lt David F. Smith	8. CONTRACT OR GRANT NUMBER(s)
9. PERFORMING ORGANIZATION NAME AND ADDRESS: AFIT Student at Auburn University	10. PROGRAM ELEMENT, PROJECT, TASK AREA & WORK UNIT NUMBERS
11. CONTROLLING OFFICE NAME AND ADDRESS: AFIT/CI, WPAFB OH 45433	12. REPORT DATE: 9 December 1976
	13. NUMBER OF PAGES: 38
14. MONITORING AGENCY NAME & ADDRESS(if different from Controlling Office)	15. SECURITY CLASS. (of this report): UNCLASSIFIED
	15a. DECLASSIFICATION/DOWNGRADING SCHEDULE

LEVEL I

16. DISTRIBUTION STATEMENT (of this Report)

Approved for Public Release, Distribution Unlimited

DDC

17. DISTRIBUTION STATEMENT (of the abstract entered in Block 20, if different from Report)

NOV 27 1978

F

18. SUPPLEMENTARY NOTES

NOV 6 1978

JOSEPH P. HIPPS, Major, USAF
Director of Information, AFIT

19. KEY WORDS (Continue on reverse side if necessary and identify by block number)

20. ABSTRACT (Continue on reverse side if necessary and identify by block number)

78 11 15 176

DD FORM 1 JAN 73 1473 EDITION OF 1 NOV 65 IS OBSOLETE

UNCLASSIFIED

SECURITY CLASSIFICATION OF THIS PAGE (When Data Entered)

SOLID-PROPELLANT GENERAL DEFORMATIONS AND THEIR EFFECTS ON MOTOR PERFORMANCE

David Franklin Smith

A Thesis

Submitted to

the Graduate Faculty of

Auburn University

in Partial Fulfillment of the

Requirements for the

Degree of

Master of Science

Auburn, Alabama

December 9, 1976

SOLID-PROPELLANT GENERAL DEFORMATIONS AND

THEIR EFFECTS ON MOTOR PERFORMANCE

David Franklin Smith

Permission is herewith granted to Auburn University to make copies of this thesis at its discretion, upon the request of individuals or institutions and at their expense. The author reserves all publication rights.

David F. Smith

Signature of Author

November 17, 1976

Date

Copy sent to:

Name	Date

VITA

David Franklin Smith, son of Norris Brandon and Edna (Brown) Smith, was born in Portsmouth, Virginia on August 9, 1948. He attended Portsmouth Public Schools and graduated from Woodrow Wilson High School, Portsmouth, in 1966. He served as an apprentice electrician for one year in the Norfolk Naval Shipyard, Portsmouth, Virginia, before enlisting in the United States Air Force. In June, 1973, he was admitted to Auburn University under the Airman Education and Commissioning Program of the Air Force and received the degree of Bachelor of Aerospace Engineering in December, 1975. He entered the Graduate School, Auburn University, in January, 1976 to pursue the degree of Master of Science in Aerospace Engineering. He married Rose, daughter of James and Rose (Notoriani) Forbes in April, 1967. He has two children, David F., Jr. and James Brandon.

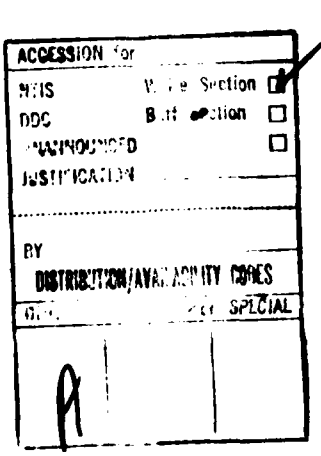

THESIS ABSTRACT

SOLID-PROPELLANT GENERAL DEFORMATIONS AND

THEIR EFFECTS ON MOTOR PERFORMANCE

David Franklin Smith

Master of Science, December 9, 1976
(B.A.E., Auburn University, 1975)

48 Typed Pages

Directed by Richard H. Sforzini

A simplified analysis of the propellant strains in solid-propellant rocket motors with circular perforated grains is presented. The analysis extends the work of Vandenkerckhove to include flexible motor cases. Each of the propellant strains is assumed independent of axial position along the propellant grain. Strains calculated from this analysis are compared with the axially varying strains obtained from the finite element analysis of Brisbane. The axial and radial strain comparisons show poor agreement for the strains predicted by this theory, however, the tangential strain correlation is excellent over a large portion of the propellant grain.

This analysis for tangential propellant strain is used to determine general propellant deformations and their effects on rocket motor internal ballistics performance predictions. Performance predictions with these deformation effects are compared with experimental

data on two rocket motors. In both cases, the performance predictions with the propellant deformation effects are closer to actual motor performance than are the predictions without the deformation effects.

TABLE OF CONTENTS

LIST OF FIGURES

LIST OF SYMBOLS

English Symbol

D	diameter
E	elastic modulus
F	force
L	grain length
M	mass
m	ratio of R_i to R_e
m_f	mass fraction; ratio of the mass of a portion of a body to the total mass of the body
P	pressure or radial stress
R	radial location in the propellant grain
r_o	burning rate of the undeformed and unheated propellant
r_c	laboratory burning rate of the propellant determined from ballistic test motors or strand burners
S	burning perimeter of the grain
T	motor thrust
T_{GR}	actual propellant temperature
T_{REF}	reference propellant temperature
Z	axial location in the propellant grain

Greek Symbol

α	linear coefficient of thermal expansion of the propellant

Δt time interval required to burn a propellant increment Δy

Δy propellant increment normal to the burning surface

ϵ strain

λ_c motor case thickness

μ ratio of R_i to R

ν Poisson's ratio

π 3.1415927..., constant

ρ density

σ stress

Subscripts

c case

e outside surface of the grain

i inside surface of the grain

o undeformed and unheated

p propellant

r radial direction

s rocket motor and payload

z axial direction

θ tangential direction

1 payload

2 forward portion of the rocket motor

3 aft portion of the rocket motor

Superscripts

' deformed grain position

I. INTRODUCTION

One of the problems in the prediction of solid propellant rocket motor performance is the variation between the actual rocket motor and laboratory propellant burning rates. In the laboratory, a sample of the solid propellant to be used in a given full scale rocket motor is burned to determine the "exact" burning rate. This is accomplished by firing a small ballistic test motor loaded with propellant or by burning a thin strand of propellant under laboratory conditions. Neither the ballistic test motor nor the strand burner technique gives consistently reliable results. The apparent burning rate of the propellant in the actual motor may be higher by 10% or more than that indicated by the strand burner or ballistic test motor.

One explanation of a portion of this burning rate discrepancy lies in the deformation of the solid propellant during motor operation. The circular perforated portion of the propellant grain in a solid propellant rocket motor (SRM) will deform due to the pressurization from the combustion chamber gases when the motor is fired. This deformation will result in a larger burning perimeter, and thus in a higher apparent burning rate. The actual burning rate of the propellant referred to a given pressure may not vary between the strand burner or ballistic test motor and the actual SRM, but the increase in burning perimeter will result in more propellant being burned in a given time interval than expected. Thus, over the total burning time of the propellant, the burning rate

seems to be higher than predicted. This variation in the apparent burning rate is directly proportional to the amount of propellant deformation at the bore of the grain.

The burning rate discrepancy is especially important on new motor designs where the "scale factor" on burning rate is unknown or uncertain. Until one or more full scale motors are fired, actual motor performance is seldom accurately predicted based on laboratory burning rate information. Thus, it is important to isolate and determine the factors that affect the burning rate determination.

In an SRM of the Space Shuttle type with a propellant web thickness of 40 inches, the initial burning bore perimeter may increase by as much as 4% due to propellant deformation, with a corresponding increase in the apparent burning rate. This example is not a limiting case and other rocket motors may show even greater deformations.

Most SRM performance prediction techniques utilize a software computer program in the design stages. The ability to incorporate the propellant deformation effects in the design of a SRM can improve the performance predictions on the new motor and perhaps point out some of the prediction errors on older motors.

It is the objective of this investigation to present a simplified analysis of the propellant deformation in SRM's. This investigation is confined to the deformations of circular perforated (c.p.) grains since many propellant grains are all or mostly c.p. In addition, due to the simplicity of the geometry, the c.p. grain is a good first test for the hypothesis with possible future efforts aimed at a strain analysis of the more complicated star or wagon wheel grain configurations.

The grain deformations predicted by this analysis are due to uniform pressure loading. Also, this analysis predicts the general deformations of the grain, as opposed to local deformations along the axis of the grain. Local deformations can be caused by end effects, pressure gradients in the combustion chamber or flight acceleration[1,2] and are not considered in this analysis.

In the present analysis, the method of Vandenkerckhove [2] for rigid motor cases has been modified to include the effects of flexible cases. In addition, an existing SRM performance prediction program is utilized to show the effect of these propellant deformations on the performance predictions for two motors. Experimental data on these two motors is compared with the performance predictions with and without the propellant deformation effects. The increased accuracy of the prediction with the deformation effects is evidence of the applicability of this investigation.

II. ANALYSIS

A tubular grain solid propellant rocket motor consists of a cylindrical body of propellant which has a circular perforation along the centerline (See Figure 1) and is enclosed by a cylindrical case. This type of solid propellant grain is usually referred to as a circular perforated or c.p. grain. When analyzing the stresses and strains in such a motor, it is convenient to model the motor as a body of propellant enclosed by a thin walled flexible case.

A section of the c.p. grain is shown in Figure 2 with the deformed and undeformed propellant surfaces as indicated. The deformation is greatly exaggerated for clarity, but the burning perimeter (S) of the propellant is seen to increase by $S\epsilon_\theta$ where ϵ_θ is the tangential strain in the propellant at the bore of the grain. The propellant deformation is symmetrical with respect to the axis along the bore of the c.p. grain and consists of a radial displacement of the grain that is constant along the circumference of the cylinder but varies along the radius. That is, the deformation is a function of radial position in the grain but at a given radius the tangential strain is a constant[3]. Also, each of the propellant strains is assumed to be independent of the axial position. The validity of this assumption will be tested when the comparison with the finite element theory of Brisbane[4] is made.

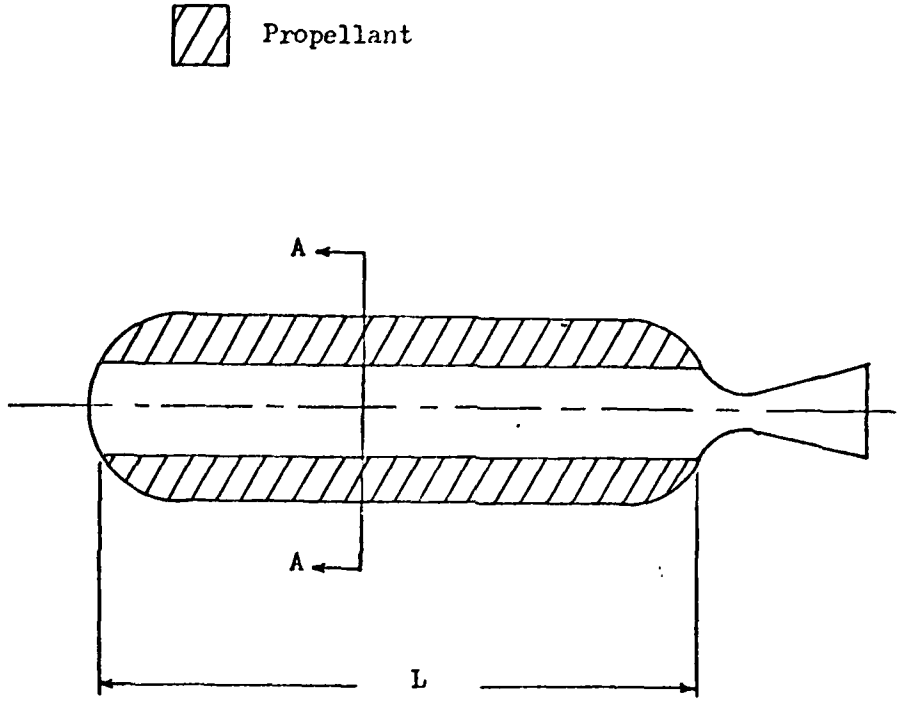

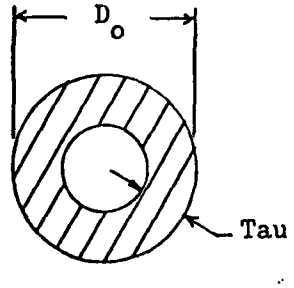

View A-A

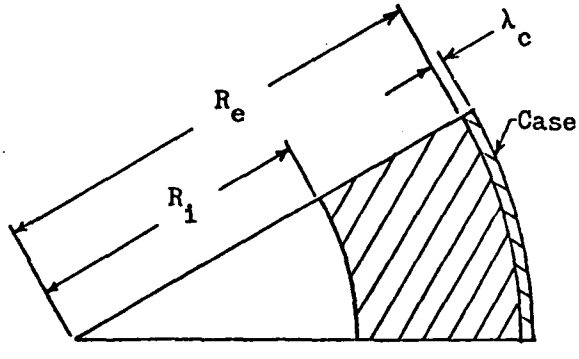

Geometry of a segment of View A-A

$\mu = R_i/R$, $m = R_i/R_e$

Figure 1. Typical Geometry of a SRM with a Circular Perforated Grain.

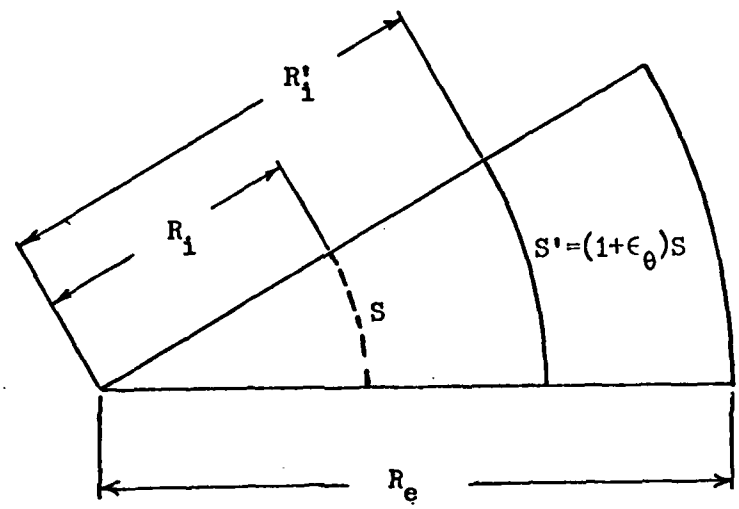

Figure 2. Cross Section Segment of a Solid Propellant Circular Perforated Grain with and without Pressurization

One may assume that the radial stress (σ_r) is essentially zero in the thin walled motor case and from the hoop stress formula the tangential stress in the motor case is given by

$$\sigma_\theta = R_e P_e / \lambda_c \tag{1}$$

where R_e is the radius of curvature of the motor case (i.e. the outside radius of the c.p. grain), λ_c is the case thickness and P_e is the radial stress in the propellant at the case wall.

For a non-rigid motor case, the tangential, radial and axial strains are non-zero and are given by Hooke's Law as

$$\epsilon_\theta = [\sigma_\theta - \nu(\sigma_r + \sigma_z)]/E \neq 0, \tag{2a}$$

$$\epsilon_r = [\sigma_r - \nu(\sigma_\theta + \sigma_z)]/E \neq 0, \tag{2b}$$

and

$$\epsilon_z = [\sigma_z - \nu(\sigma_\theta + \sigma_r)]/E \neq 0. \tag{2c}$$

In Equations (2a) through (2c), the subscripts θ, r and z refer to tangential, radial and axial directions, respectively. The strains are denoted by ϵ, the stresses by σ, the elastic modulus by E and Poisson's ratio by ν.

If the rocket motor were a closed pressure vessel, then the axial stress in the case would simply be one half of the hoop stress (See Figure 3), however, in a rocket motor the situation is not as simple. There is a uniform pressure force on the head end of the motor and a non-uniform pressure force on the case shoulders forward of the throat and in the exit cone of the nozzle. For the purpose of a static anal-

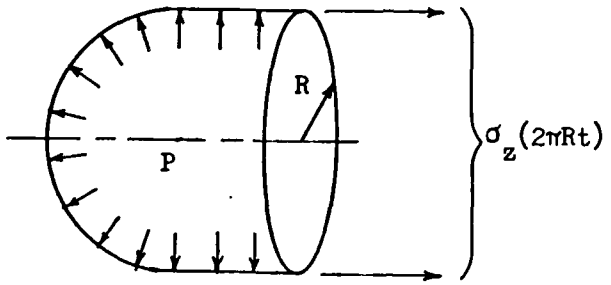

$$\sigma_z(2\pi Rt) = P(\pi R^2)$$

$$\sigma_z = PR/(2t)$$

Figure 3. Half Section of a Closed Pressure Vessel with a Uniform Internal Pressure (P).

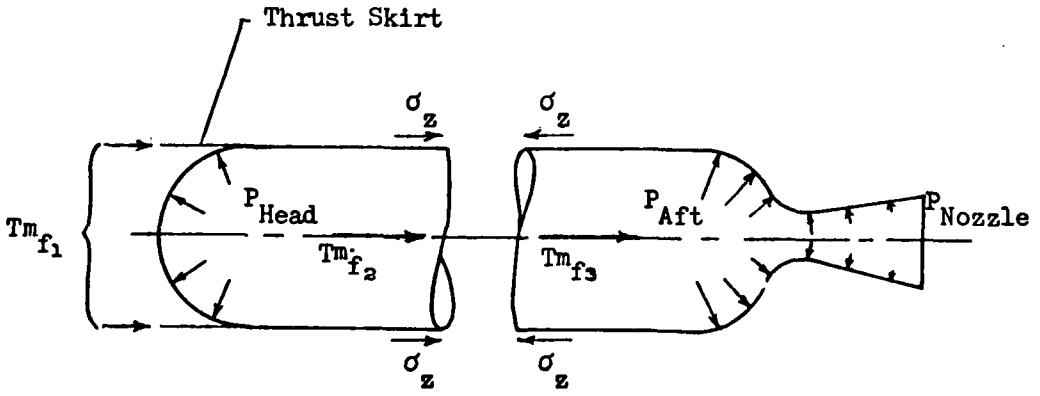

$$\sigma_z(2\pi\lambda_c R) = P_{Head}(\pi R^2) - T(m_{f_1})$$

$$m_{f_1} = M_1/M_s \qquad m_{f_2} = M_2/M_s \qquad m_{f_3} = M_3/M_s$$

$$M_s = M_1 + M_2 + M_3$$

Figure 4. Free-Body Diagram of a Typical SRM.

ysis, there are also reverse effective forces acting through the center of gravity of the body equal in magnitude to the motor thrust (T) times the mass fraction (m_f) of that portion of the body. In Figure 4, M indicates mass and m_f indicates the mass fraction which is the mass of a portion of the body divided by the total mass of the body. The subscripts 1, 2, 3 and s indicate the payload, forward portion of the body, aft portion of the body and the entire vehicle, respectively. For example, the reverse effective force acting on the thrust skirt is equal in magnitude to the mass fraction of the payload (m_{f_1}) times the motor thrust. It is obvious that a rigorous analysis of the axial stress in the motor case becomes very complicated, since this stress is a function of both time and position along the axis of the motor (i.e. the mass fraction of the free body will be different at every axial location, and the pressure and thrust may both be functions of time).

It is desirable to choose a constant axial case stress for the purpose of simplifying this analysis while observing that the case strain than most greatly affects the propellant bore strain will be the tangential motor case strain. The propellant has essentially a constant volume, since Poisson's ratio is close to 0.5 for most composite solid propellants. Therefore, a tangential case strain that causes a small change in case diameter, and thus a small change in the outside diameter of the case-bonded grain, will produce a somewhat larger increase in the grain bore diameter. The axial case strain not only has a smaller effect on the grain bore deformation for a given strain, it is also smaller in magnitude than the tangential case strain. Thus, the validity of any assumption on the axial case stress must be considered with

respect to the effect on the tangential motor case strain. It is also important to note that the effect on the propellant deformation at the bore of the grain from any of the motor case strains will be small compared to the deformations due to the internal pressure loading.

The minimum axial case stress (assuming that the motor case is always in tension) would be zero and a clear maximum would be one half of the hoop stress (since this corresponds to a closed pressure vessel). An application of Hooke's Law for the situation where the axial motor case stress is zero and with a nominal value of 0.3 for ν of the case yields (for $\sigma_{zc} = \sigma_{rc} = 0$)

$$E_c \epsilon_{zc} = -0.3\, \sigma_{\theta c} \tag{3a}$$

and

$$E_c \epsilon_{\theta c} = \sigma_{\theta c}, \tag{3b}$$

where the c subscript refers to the motor case. For a maximum axial case stress of one half of the hoop stress, we have (for $\sigma_{zc} = 0.5\, \sigma_{\theta c}$ and $\sigma_{rc} = 0$)

$$E_c \epsilon_{zc} = 0.5\, \sigma_{\theta c} - 0.3(\sigma_{\theta c}) = 0.2\, \sigma_{\theta c} \tag{3c}$$

and

$$E_c \epsilon_{\theta c} = \sigma_{\theta c} - 0.3(0.5\, \sigma_{\theta c}) = 0.85\, \sigma_{\theta c}. \tag{3d}$$

Comparing Equations (3b) and (3d), one sees that the tangential case strain changes only 15% between the maximum and minimum assumed values for the axial case stress. We thus have a small change in a quantity that has a small effect on the propellant deformation. In addition, the maximum axial case stress assumed in this argument is clearly

greater than any real axial case stress. Thus, by assuming a zero axial motor case stress, one may expect an even smaller change in the tangential case strain and a resulting minor difference in the actual propellant deformation at the bore of the grain. It should also be noted, as shown in Figure 4, that for high acceleration vehicles (i.e. high thrust to weight ratio) the axial case stress may well be close to zero.

For the thin walled case, with the radial and axial stresses assumed to be zero, Equations (2a) through (2c) are rewritten as

$$\epsilon_{\theta c} = \sigma_{\theta c}/E_c, \tag{4a}$$

$$\epsilon_{rc} = -\nu_c \sigma_{\theta c}/E_c, \tag{4b}$$

and

$$\epsilon_{zc} = -\nu_c \sigma_{\theta c}/E_c. \tag{4c}$$

With Equation (1), one may further modify Equations (4) to become

$$\epsilon_{\theta c} = R_e P_e/(E_c \lambda_c), \tag{5a}$$

$$\epsilon_{rc} = -\nu_c R_e P_e/(E_c \lambda_c), \tag{5b}$$

and

$$\epsilon_{zc} = -\nu_c R_e P_e/(E_c \lambda_c). \tag{5c}$$

Assuming that the propellant is bonded to the case, the strains at the outer radius of the propellant grain must be the same as the case strains at that surface. So, combining Equations (2a), (2c), (4a) and (4c), we have

$$[\sigma_{\theta p} - \nu_p(\sigma_{rp} + \sigma_{zp})]/E_p = \epsilon_{\theta p} = \epsilon_{\theta c} = R_e P_e/(E_c \lambda_c) \tag{6a}$$

and

$$[\sigma_{zp} - \nu_p(\sigma_{rp} + \sigma_{\theta p})]/E_p = \epsilon_{zp} = \epsilon_{zc} = -\nu_c R_e P_e/(E_c \lambda_c), \qquad (6b)$$

where the p subscript refers to the propellant. Solving Equations (6a) and (6b) for the axial propellant stress (σ_{zp}) at the propellant-case interface, one obtains

$$\sigma_{zp} = [\sigma_{\theta p} - \nu_p \sigma_{rp} - E_p R_e P_e/(E_c \lambda_c)]/\nu_p \qquad (7a)$$

and

$$\sigma_{zp} = \nu_p \sigma_{rp} + \nu_p \sigma_{\theta p} - \nu_c E_p R_e P_e/(E_c \lambda_c). \qquad (7b)$$

Equating (7a) and (7b) yields

$$[\sigma_{\theta p} - \nu_p \sigma_{rp} - E_p R_e P_e/(E_c \lambda_c)]/\nu_p = \nu_p(\sigma_{rp} + \sigma_{\theta p}) - \nu_c E_p R_e P_e/(E_c \lambda_c) \qquad (8)$$

which reduces to

$$\sigma_{\theta p}(1 - \nu_p^2) - \nu_p \sigma_{rp}(1 + \nu_p) = E_p R_e P_e (1 - \nu_c \nu_p)/(E_c \lambda_c). \qquad (9)$$

The radial and tangential stresses in the propellant (σ_{rp} and $\sigma_{\theta p}$, respectively) may also be determined from the Lamè equations for a c.p. grain[2]:

$$\sigma_{rp} = [m^2 P_i - P_e + \mu^2(P_e - P_i)]/(1 - m^2) \qquad (10a)$$

and

$$\sigma_{\theta p} = [m^2 P_i - P_e - \mu^2(P_e - P_i)]/(1 - m^2), \qquad (10b)$$

where m is the ratio of the inside radius to the outside radius, μ is the ratio of the inside radius to any other radius (See Figure 1), P_i is the pressure at the bore of the grain and P_e is the radial stress at the outside radius of the grain.

Evaluating Equations (10a) and (10b) at the outside radius of the grain (at the case wall where $\mu = R_i/R_e = m$), one obtains

$$\sigma_{rp_e} = [m^2P_i - P_e + m^2(P_e - P_i)]/(1 - m^2)$$

$$= -P_i \tag{11a}$$

and

$$\sigma_{\theta p_e} = [m^2P_i - P_e - m^2(P_e - P_i)]/(1 - m^2)$$

$$= [2m^2P_i - P_e(1 + m^2)]/(1 - m^2). \tag{11b}$$

Substituting Equations (11a) and (11b) into Equation (9) yields

$$[2m^2P_i - P_e(1 + m^2)](1 - \nu_p^2)/(1 - m^2) + \nu_p P_e(1 + \nu_p) =$$

$$E_p R_e P_e(1 - \nu_c\nu_p)/(E_c\lambda_c), \tag{12}$$

which may be written in terms of the radial stress (P_e) at the propellant-case interface as

$$P_e/P_i = \frac{(2m^2)(1 - \nu_p^2)/(1 - m^2)}{E_p R_e(1-\nu_c\nu_p)/(E_c\lambda_c) - \nu_p(1+\nu_p) + (1-\nu_p^2)(1+m^2)/(1-m^2)}. \tag{13}$$

In Equation (13), P_e/P_i is referred to as the pressure ratio, where P_e may be considered as a fictitious pressure applied to the outside surface of the grain and equal in magnitude to the radial stress at that surface. With an assumed uniform internal pressure, P_e will be uniform along the axis of the grain.

To determine the bore stresses of the propellant, Equations (10a) and (10b) are evaluated at the bore of the grain (where $\mu = 1$) to give

$$\sigma_{rp_i} = [m^2 P_i - P_e + (P_e - P_i)]/(1 - m^2)$$

$$= -P_i \qquad (14a)$$

and

$$\sigma_{\theta p_i} = [m^2 P_i - P_e - (P_e - P_i)]/(1 - m^2)$$

$$= [P_i(1 + m^2) - 2P_e]/(1 - m^2). \qquad (14b)$$

The external pressure on the grain (P_e) varies only slightly from the internal pressure (P_i) and is constant along the length of the grain for an assumed uniform internal pressure. That is, the pressure ratio defined by Equation (13) is approximately one and is not a function of axial location in the grain. Neglecting end constraints, the end loading will be approximately equal in magnitude to the internal pressure. In the actual rocket motor, even without end constraints, there will be shear stresses at the propellant-case interface and the axial propellant stress will be a function of axial location. For the current analysis, these shear stresses are not considered and the grain is under an essentially uniform pressure loading as shown in Figure 5. The axial propellant stress (σ_{zp}) is then approximately equal to the internal pressure and is assumed constant across the radius of the grain and along the axis of the grain. For the case-bonded grain, the propellant and case strains were matched. For consistency, the axial propellant stress is evaluated at the propellant-case interface from Equation (7b):

$$\sigma_{zp} = \nu_p \sigma_{rp_e} + \nu_p \sigma_{\theta p_e} - \nu_c E_p R_e P_e/(E_c \lambda_c). \qquad (15)$$

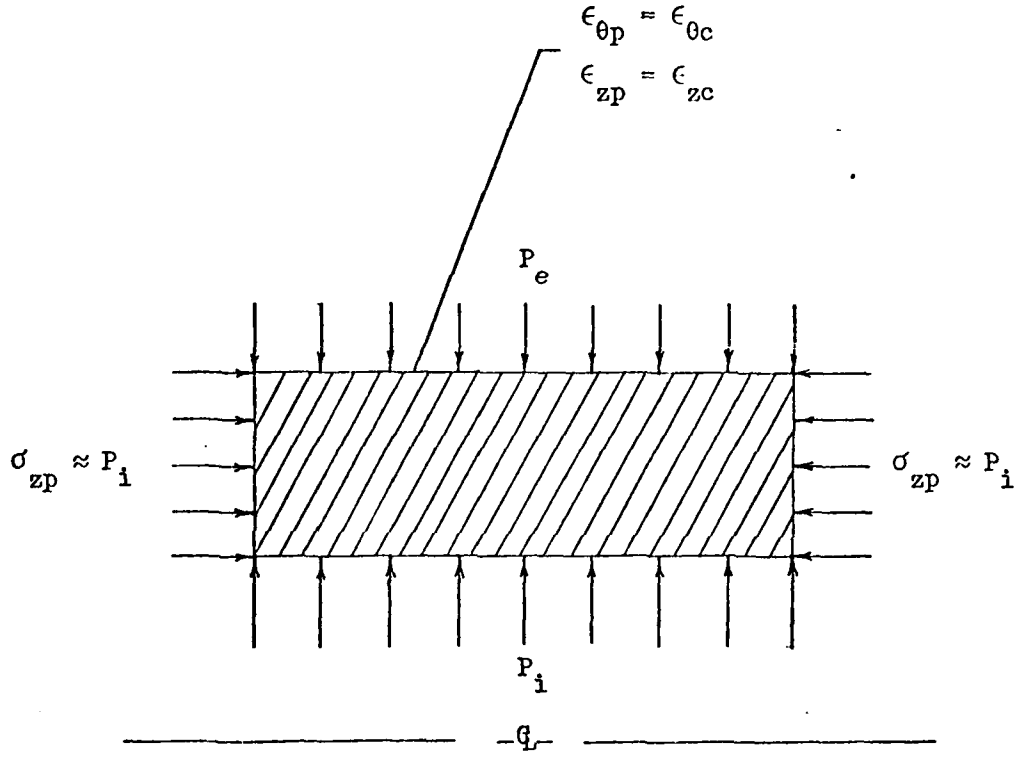

Figure 5. Pressure Distribution on the SRM Propellant Grain.

Equation (15) is a function of the geometry, physical properties of the propellant and motor case, and the pressure ratio. In addition, the axial stress in the propellant is independent of axial position. Substituting the radial and tangential propellant stresses at the case wall given by Equations (11a) and (11b) into Equation (15) gives

$$\sigma_{zp} = -\nu_p P_e + \nu_p[2m^2P_i - P_e(1 + m^2)]/(1 - m^2) - \nu_c E_p R_e P_e/(E_c \lambda_c). \quad (16)$$

The bore strains of the propellant can be determined from Hooke's Law, Equations (2a) through (2c), in terms of the bore stresses and the physical properties of the propellant and are

$$E_p \epsilon_{\theta p_i} = \sigma_{\theta p_i} - \nu_p(\sigma_{rp_i} + \sigma_{zp}), \quad (2a)$$

$$E_p \epsilon_{rp_i} = \sigma_{rp_i} - \nu_p(\sigma_{\theta p_i} + \sigma_{zp}), \quad (2b)$$

and

$$E_p \epsilon_{zp_i} = \sigma_{zp} - \nu_p(\sigma_{\theta p_i} + \sigma_{rp_i}). \quad (2c)$$

Substituting Equations (14a) and (14b) into Equation (2a) gives

$$E_p \epsilon_{\theta p_i} = [P_i(1+m^2)-2P_e]/(1-m^2)+\nu_p P_i+\nu_p{}^2 P_e -$$
$$\nu_p{}^2[2m^2P_i-P_e(1+m^2)]/(1-m^2)+\nu_p \nu_c E_p R_e P_e/(E_c \lambda_c). \quad (17)$$

After grouping coefficients of P_i and P_e, Equation (17) may be written as

$$E_p \epsilon_{\theta p_i} = P_i[(1+m^2)/(1-m^2)+\nu_p-(2m^2\nu_p{}^2)/(1-m^2)] +$$
$$P_e\{-2/(1-m^2)+\nu_p{}^2[1+(1+m^2)/(1-m^2)]+\nu_p \nu_c E_p R_e/(E_c \lambda_c)\}. \quad (18)$$

Finally, the bore strain in terms of the pressure ratio, geometry and physical properties is given by

$$\epsilon_{\theta p_i} = (P_i/E_p)\{[1+m^2+\nu_p(1-m^2-2m^2\nu_p^2)]/(1-m^2) + (P_e/P_i)[2(\nu_p^2-1)/(1-m^2)+\nu_p\nu_c E_p R_e/(E_c\lambda_c)]\}. \quad (19)$$

The radial and axial bore strains are determined in a similar fashion. Substituting Equations (14a), (14b) and (16) into Equation (2b) yields

$$E_p\epsilon_{rp_i} = -P_i-\nu_p[P_i(1+m^2)-2P_e]/(1-m^2)+\nu_p^2P_e - \nu_p^2[2m^2P_i-P_e(1+m^2)]/(1-m^2)+(\nu_p\nu_c E_p R_e P_e)/(E_c\lambda_c), \quad (20)$$

which reduces to

$$E_p\epsilon_{rp_i} = P_i[-1-\nu_p(1+m^2)/(1-m^2)-2m^2\nu_p^2/(1-m^2)] + P_e[2\nu_p/(1-m^2)+\nu_p^2+\nu_p^2(1+m^2)/(1-m^2)+\nu_p\nu_c E_p R_e/(E_c\lambda_c)]. \quad (21)$$

In final form, the radial bore strain is

$$\epsilon_{rp_i} = (P_i/E_p)\{-[\nu_p(1+m^2+2m^2\nu_p)/(1-m^2) + 1] + (P_e/P_i)[2\nu_p(1+\nu_p)/(1-m^2)+\nu_p\nu_c E_p R_e/(E_c\lambda_c)]\}. \quad (22)$$

Substituting Equations (14a), (14b) and (16) into Equation (2c) gives

$$E_p\epsilon_{zp_i} = -\nu_p P_e + \nu_p[2m^2P_i-P_e(1+m^2)]/(1-m^2) - \nu_c E_p R_e P_e/(E_c\lambda_c) + \nu_p P_i - \nu_p[P_i(1+m^2)-2P_e]/(1-m^2). \quad (23)$$

After grouping coefficients of P_i and P_e in Equation (23), we have

$$E_p \epsilon_{zp_i} = P_i\{2m^2\nu_p/(1-m^2) + \nu_p[1-(1+m^2)/(1-m^2)]\} +$$

$$P_e\{2\nu_p/(1-m^2)-\nu_p[1+(1+m^2)/(1-m^2)]-\nu_c E_p R_e/(E_c \lambda_c)\}. \quad (24)$$

Equation (24) then simplifies to yield the axial bore strain of the propellant:

$$\epsilon_{zp_i} = -[\nu_c P_i R_e/(E_c \lambda_c)](P_e/P_i). \quad (25)$$

Note that by expressing the axial strain in the above fashion, it is not necessary to know the radial stress at the propellant-case interface (P_e). Instead, the internal pressure (combustion chamber pressure) and the pressure ratio are required. The pressure ratio is a function only of the geometry and physical properties of the propellant and motor case, so the axial propellant strain is indcpendent of axial position in the grain.

Equations (19), (22) and (25) give the tangential, radial and axial strains, respectively, at the bore of the propellant grain subject to the constraints and assumptions of this analysis. Each of these three relations is independent of axial position and is a function only of the geometry, physical properties of the propellant and motor case and the chamber pressure of the rocket motor.

III. COMPARISON WITH THE FINITE ELEMENT ANALYSIS

The results of this simplified analysis of propellant strains are summarized in Figures 6 through 11. The strain of major importance to propellant deformation is the tangential strain as was mentioned in the Analysis section of this paper, however, the radial and axial strain results are also shown. It is necessary to examine each of the three strain results so that a valid conclusion may be drawn about the entire analysis.

Each of the six plots is shown in non-dimensional form with the strain plotted as a function of axial location along the propellant grain. The solid lines indicate the theory developed in this paper and the symbols represent the finite element solution of Brisbane[4]. The propellant grains used for these results are 140 inch diameter c.p. grains with an axial length of 300 inches and initial web thicknesses of 40, 34, 28, 22, 16 and 10 inches. The results shown are for these configurations, but they may be applied to any motor with the same non-dimensional parameters. Each of the three strains has six plots associated with it. Each of these six plots represents a different initial web thickness (TAU) which is expressed in the non-dimensional form of web thickness divided by the outside diameter of the grain (DO). The independent variable for each plot is the ratio of axial location (Z) to the outside diameter of the grain. The axial location on the grain

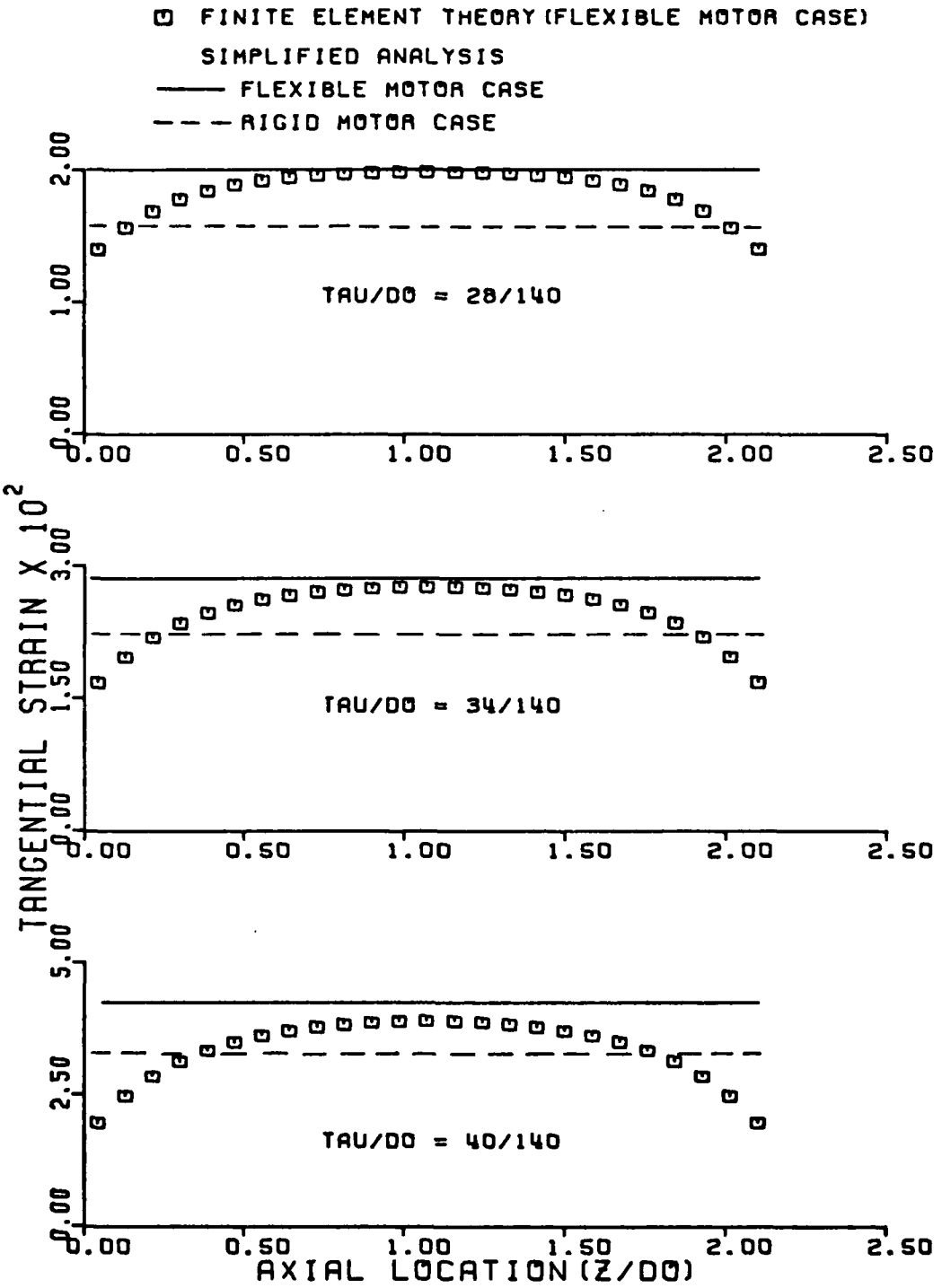

Figure 6. Comparison of the Finite Element Theory and Simplified Analysis Results for Tangential Bore Strain.

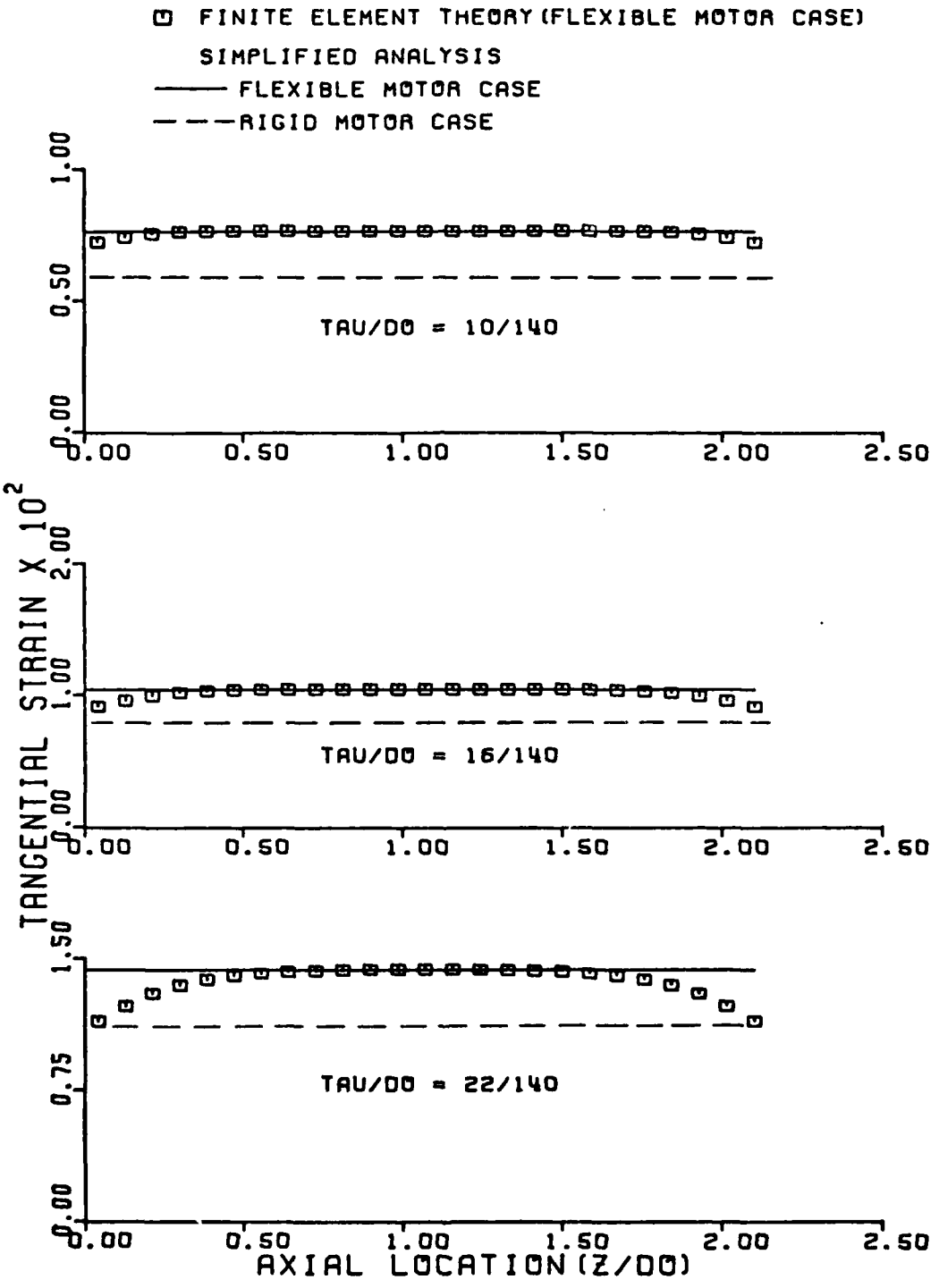

Figure 7. Continued Comparison of the Finite Element Theory and Simplified Analysis Results for Tangential Bore Strain.

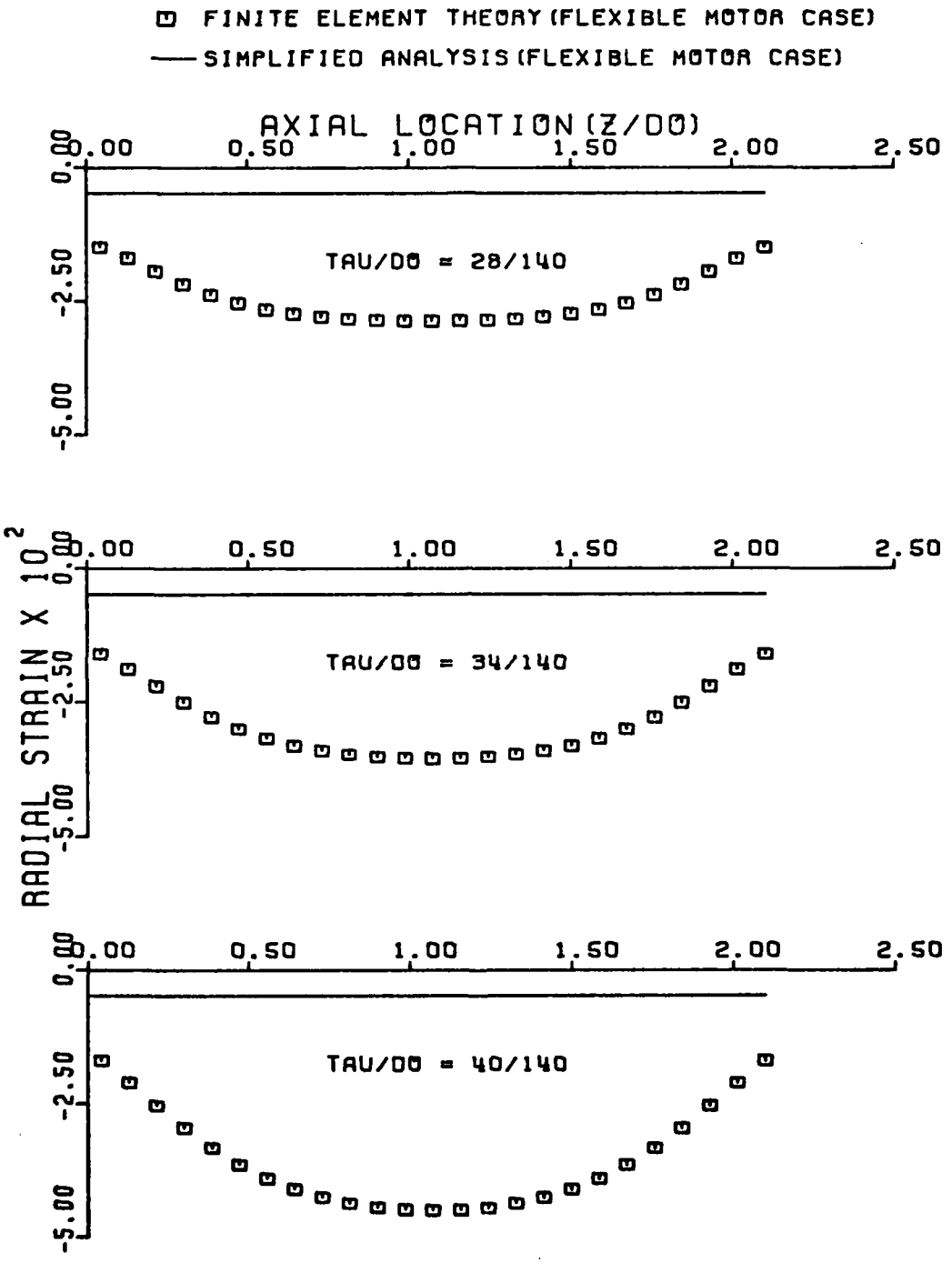

Figure 8. Comparison of the Finite Element Theory and Simplified Analysis Results for Radial Bore Strain.

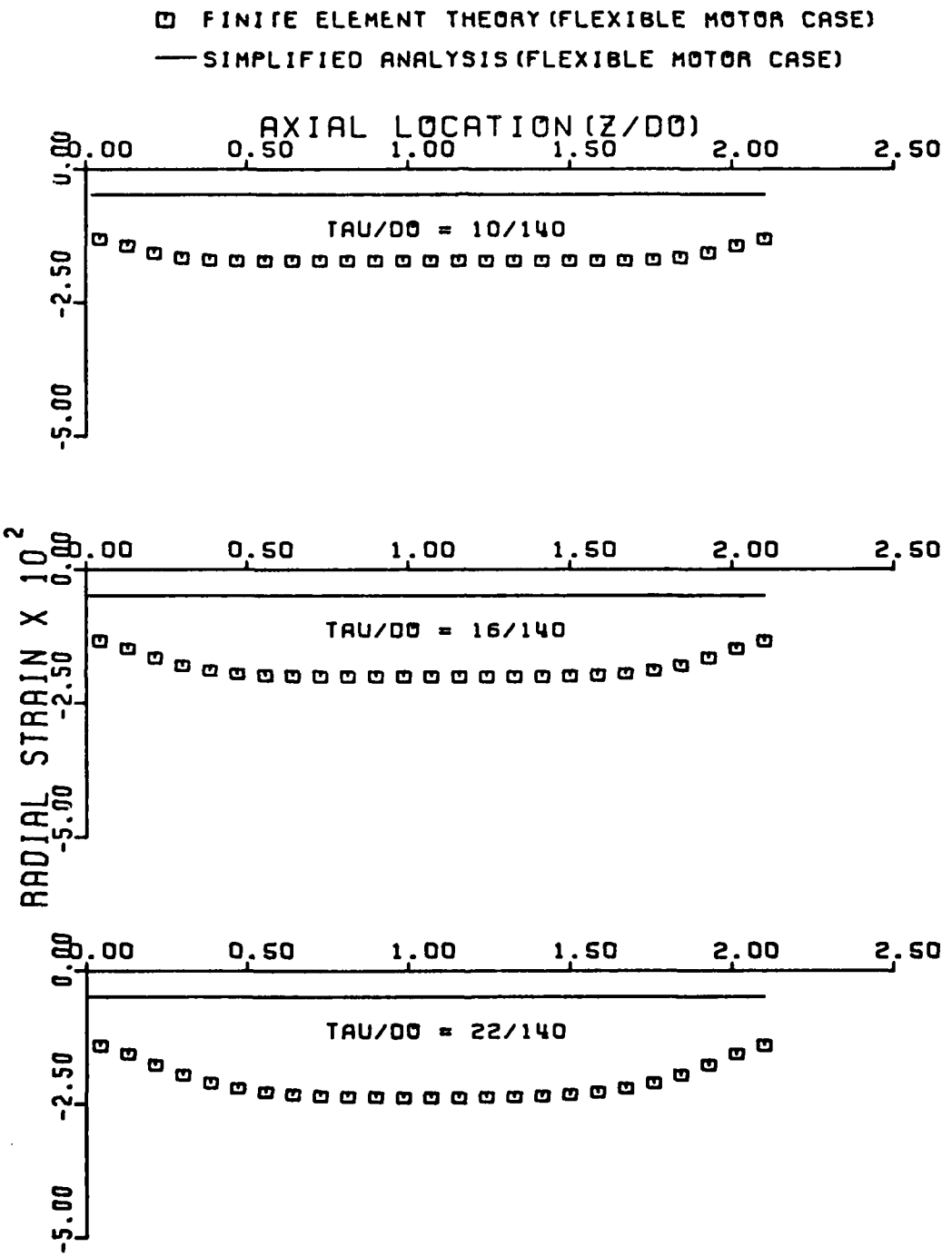

Figure 9. Continued Comparison of the Finite Element Theory and Simplified Analysis Results for Radial Bore Strain.

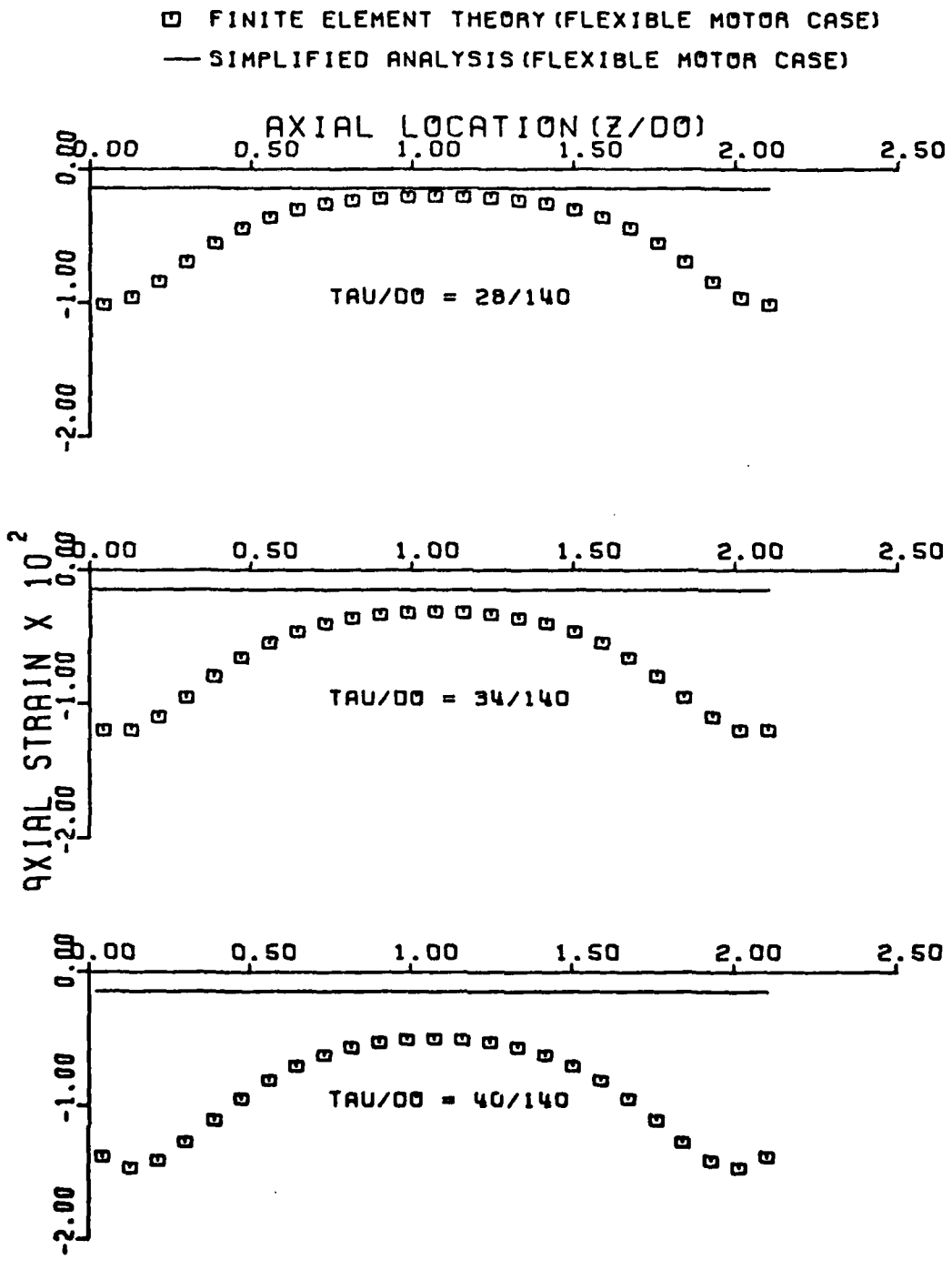

Figure 10. Comparison of the Finite Element Theory and Simplified Analysis Results for Axial Bore Strain.

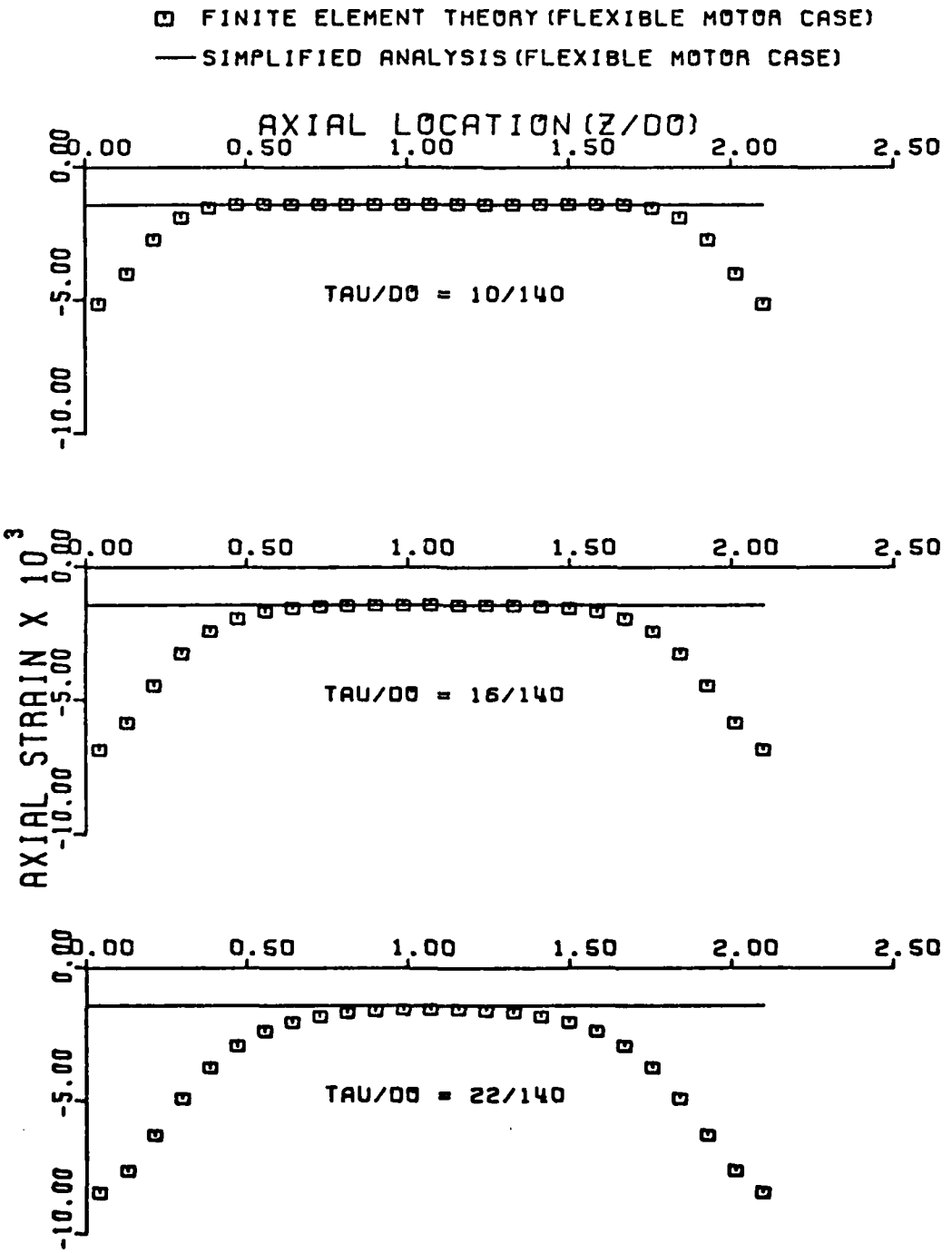

Figure 11. Continued Comparison of the Finite Element Theory and Simplified Analysis Results for Axial Bore Strain.

may be measured from either the head or aft end of the grain since the propellant deformation is symmetric about the midpoint of the axial length of the grain. Each of the six figures shows the strains predicted by this theory to be independent of axial location, while the results of Brisbane are definite functions of axial position.

The tangential strain plots (Figures 6 and 7) show results for the six configurations used in this analysis. The worst comparison occurs for the largest web to outside diameter ratio of 40/140. For this example, the simplified strain analysis gives a tangential strain that is greater than, but within 10% of, the finite element results over approximately one quarter of the length of the grain. The results improve dramatically for the smaller web to outside diameter ratios. At the smallest web thickness (10 inches), the strain predicted by this analysis is less than 0.5% lower than the results from the finite element solution over 65% of the length of the grain. For this case, the tangential strain at the ends of the grain (where the largest difference is expected due to the uniform end loading assumed in this analysis) is still less than 6% greater than the "exact" strain.

The dashed lines on Figures 6 and 7 represent the results obtained for the tangential propellant strain from Vandenkerckhove's[2] analysis for the rigid motor case. Vandenkerckhove expressed his results in terms of the radial and tangential propellant stresses. His analysis is extended in the same manner as this analysis to obtain the tangential bore strain of the propellant. The motor case and propellant strains are matched at the propellant-case interface and are zero for the rigid motor case. A uniform end loading equal in magnitude to the

internal pressure (P_i) is assumed (i.e. Vandenkerckhove modeled the grain as a long, uniform thick walled cylinder with no end loading or end constraints) and the tangential strain is given as a function of the pressure ratio and the physical properties of the propellant. The tangential strain predicted by the rigid motor case analysis is not, however, a function of the physical properties of the motor case as is true for the flexible motor case analysis.

As seen in Figures 6 and 7, the tangential strains calculated from the rigid motor case analysis are generally less than the finite element results, while the flexible motor case results are larger. The tangential strains predicted by the current theory are closer to the finite element results than are the rigid case results for the middle portion of the grain in each of the six configurations. For the larger webs (Figure 6), the rigid case results are better than the flexible case results near the ends of the grain, but this difference is less pronounced for the smaller webs. In general, except for locations very close to the ends of the grain, the flexible motor case predictions of this analysis yield a better approximation to the finite element results.

The results for radial and axial strains are not as promising as those for the tangential strain. The axial propellant strains predicted by the present theory are close to the strains predicted by the finite element solution for the smallest webs (Figure 11), but in general, the results of this analysis must be deemed invalid for both radial and axial strains. In particular, the radial strains (Figures 8 and 9) predicted by this simplified analysis are greatly in error when compared to the results obtained from the finite element method. This does not

invalidate the analysis for application to the problem at hand, since the results for tangential strain, the only parameter needed for the ballistic analysis, are sufficiently close to the "exact" strains that they may be used to include propellant deformation effects in motor performance predictions.

The advantage of this analysis, at least for tangential strain, lies in the simplicity of the calculations required. Whereas the finite element technique gives more accurate results, it requires lengthy computer time and storage to complete. The tangential strain computed from the equations derived in this analysis requires only a knowledge of the geometry and physical properties of the motor and is done in fractions of a second on the computer.

In summary, this simplified analysis for propellant strains yields good results for tangential strain calculations and is directly applicable as a first approach to including deformation effects in rocket motor performance predictions. Since the propellant deformation effects require a tangential bore strain calculation after each propellant increment is burned, the disadvantage of the finite element technique is obvious. The entire analysis would have to be repeated at each bore diameter and each such analysis requires substantial time to complete. The tangential strain calculations from this simplified analysis also have to be repeated at each bore diameter, but they require only the evaluation of one relatively simple equation. This analysis thus provides a fast, simple technique for calculating tangential strain which may be easily included in existing software computer programs in order to evaluate the effect of propellant deformations in rocket motors.

IV. APPLICATIONS TO THE INTERNAL BALLISTICS OF SOLID ROCKET MOTORS

As was discussed in the Introduction section of this thesis, the propellant deformations in solid rocket motors can greatly affect motor performance and performance predictions. A detailed analysis of the effect of grain deformation on the internal ballistics of solid rocket motors is presented in Reference 5.

The basic hypothesis upon which the grain deformation effects on internal ballistics is based is that, at constant pressure, the regression rate of the propellant burning surface is independent of the strain in the solid propellant underneath the burning layer. In addition, when Poisson's ratio is approximately 0.5 (as is true for most composite solid propellants) it can be shown that the density of the unheated propellant is essentially independent of strain[5]. The unheated propellant is that portion of the grain which lies under the burning surface of the grain. This thin layer of burning propellant is of unknown composition (liquid and/or solid) and the physical properties of the propellant in this zone are degraded to a state where they cannot support shear stress[5]. Thus, the density and burning rate of the propellant within the burning perimeter are considered independent of the strain in the propellant beneath the combustion zone.

The internal ballistics of the SRM are modified for propellant deformation effects by two changes. The mass generated equation and the time interval required to burn a given increment of propellant are both

modified. The following discussion is taken from the work of Sforzini and Foster and is only summarized. The reader is referred to Reference 6 for a detailed discussion of the SRM performance prediction program. Only the analysis of the deformation effects on internal ballistics are considered here. The program modifications necessary to include these effects are explained in Reference 5.

The mass generated per unit time per unit length at the burning surface of the propellant (the control surface is chosen to lie just beneath the layer of degraded propellant) would normally be written as

$$\dot{m}_G/L = S_o \rho_{po} r_o \tag{26}$$

where S_o is the burning perimeter of the grain, ρ_{po} is the density of the propellant and r is the burning rate of the propellant. The subscript o refers to the undeformed and unheated propellant. The deformation modification requires that Equation (26) be written as

$$\dot{m}_G/L = S_o(1 + \epsilon_\theta)\rho_{po} r_c / \{[1 - P(1 - 2\nu)/E][1 + \alpha(T_{GR} - T_{REF})]\}^3 \tag{27}$$

where ϵ_θ is the tangential strain in the propellant just beneath the burning surface (calculated from the tangential strain relation derived in the Analysis section of this paper), P is the chamber pressure, E is the elastic modulus of the propellant and ν is Poisson's ratio for the propellant. The term $[1+\alpha(T_{GR}-T_{REF})]$ is a further modification for the thermal expansion effects in the grain. The linear coefficient of thermal expansion of the propellant is α, and T_{REF} and T_{GR} are reference and actual temperatures, respectively. Equation (27) is presented exactly as found in Reference 5. The thermal effect is a very small one and is

not directly connected with the propellant deformation due to pressurization. Also, it is assumed that thermal and pressure loadings have negligible effects on changes in the grain length (See Reference 5).

The time interval (Δt) required to burn a propellant increment (Δy) normal to the burning perimeter is calculated from

$$\Delta t = \Delta y / r_o . \tag{28}$$

The effect of propellant deformation due to pressurization and heating will modify the burning rate as

$$r_o = r_c (1 + \epsilon_\theta) / \{ [1 - P(1 - 2\nu)/E][1 + \alpha(T_{GR} - T_{REF})] \}^3 \tag{29}$$

where r_c is the propellant burning rate determined from ballistic test motors or strand burners. The time interval of Equation (28) is thus modified to include the effect of the deformed propellant by using Equation (29) for the burning rate.

Using the SRM performance prediction program of Reference 5, the effect of the propellant deformations due to pressure loading are examined for two motors. Detailed descriptions of the motors and the input parameters for the deformation analysis are given in Reference 5. The thermal expansion effects are not present for either of these test cases since the reference and actual temperatures are the same. The performance program is used with and without the propellant deformation modifications and the results are compared with experimental data on the two motors. These results are shown in Figures 12 and 13.

Figure 12 shows a plot of vacuum thrust versus time for a Castor motor developed by the Thiokol Chemical Corporation (motor designation

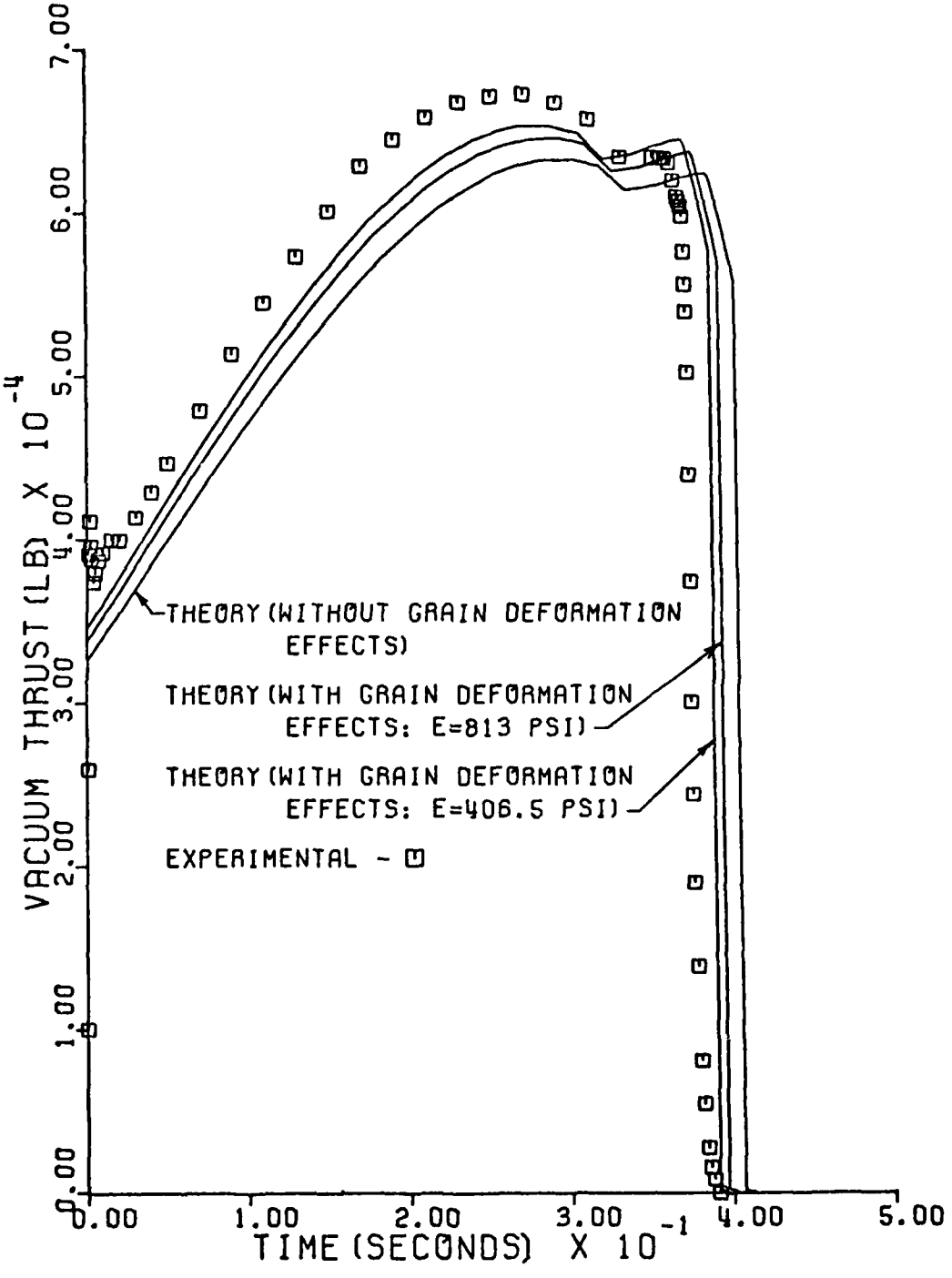

Figure 12. Comparison of Experimental and Theoretical Results for a Castor TX354-5 SRM.

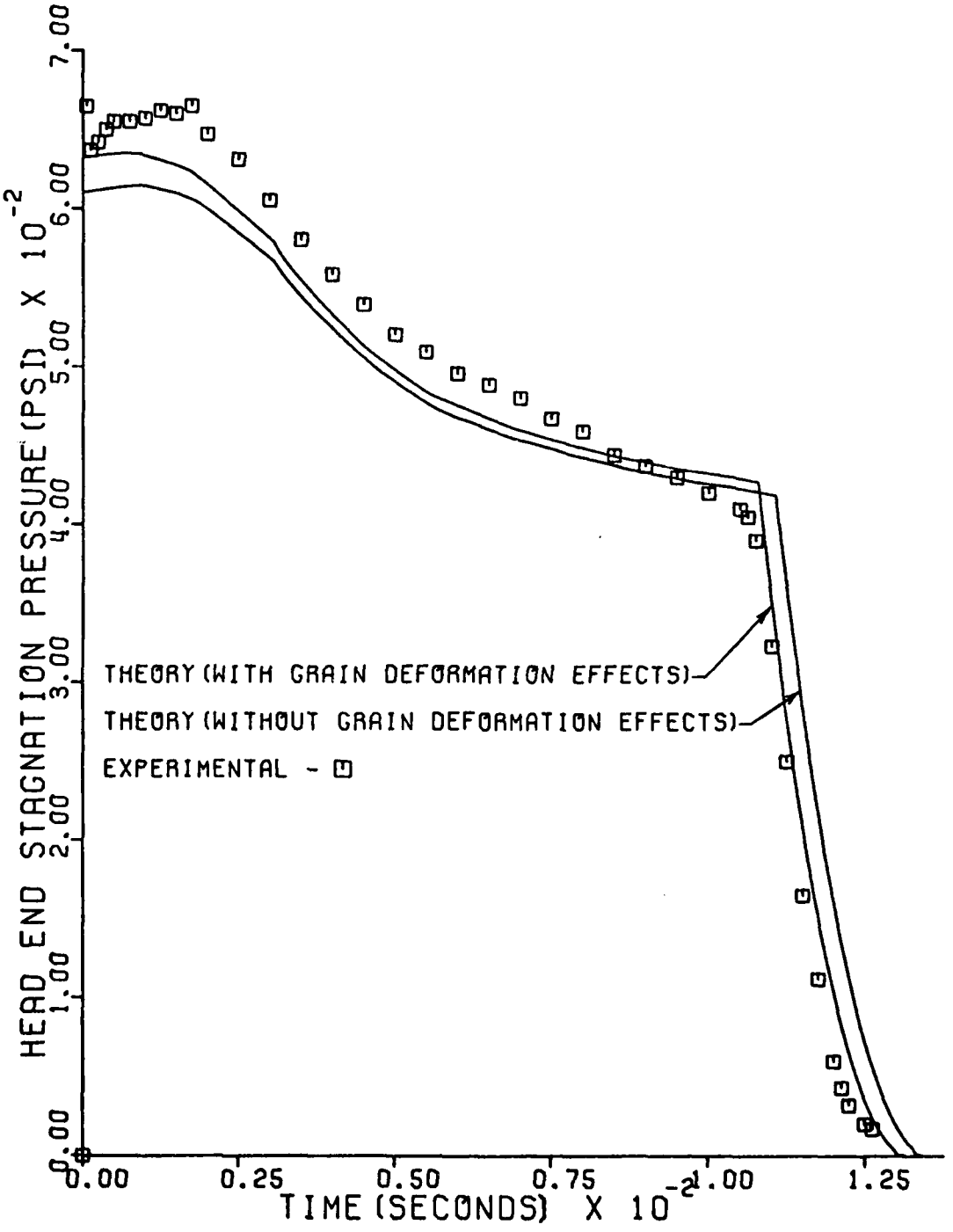

Figure 13. Comparison of Experimental and Theoretical Results for a Titan III C/D SRM.

TX354-5). This motor has a totally c.p. slotted grain and is thus especially suited for a test case on the results of this analysis. Figure 12 includes the experimental results obtained from Thiokol[7] and the results predicted by three predictions of the SRM performance prediction program. Two of these predictions include the propellant deformation effects while the third does not. The two predictions that include the deformation effects differ only in the elastic modulus (E) of the propellant. The nominal modulus is 813 psi., but the second computer run was made with a modulus of 406.5 psi. to demonstrate the effects of the propellant modulus on the performance of the rocket motor. These effects may be important for a particular application since the elastic modulus may vary between propellant batches and the actual modulus may be uncertain.

As can be seen from Figure 12, the two performance predictions that include the deformation effects more closely predict the actual motor performance. The prediction with the low modulus serves to point out the definite effects of propellant modulus on the performance predictions. This is evident since the modulus of the propellant affects only the deformation modifications in the performance prediction program. As the elastic modulus decreases, the propellant will deform more under pressurization. This will result in a larger actual burning surface. Thus, the apparent burning rate will increase resulting in a larger deviation from the expected burning rate based on ballistic test motor or strand burner data.

Each of the three performance predictions of Figure 12 was made without a scale factor on the strand burning rate. The performance prediction

with deformation effects and the low elastic modulus (E=406.5 psi.) comes closer to the motor performance than does the prediction with the deformation effects and the nominal modulus (E=813 psi.). In the case of two or more SRM's firing in parallel, variations in performance will contribute to thrust imbalance. The effect of the propellant modulus on the deformation of the grain, and thus on motor performance, can be helpful when investigating such phenomena since the physical properties of the propellant may vary somewhat between motors.

Figure 13 shows the predictions for the Titan III C/D SRM where head end stagnation pressure is plotted versus time. Again, no scale factor was used on the burning rate and the performance prediction with the deformation effect is closer to the experimental data than the results without the deformation effects. This motor has a star grain segment at the head end of the grain but this segment is treated with a burning rate that is not modified due to the propellant deformation. The present strain analysis is not applicable to star grains, and for that reason, no deformation effects are included for this portion of the grain. This probably has a minor effect on the performance predictions for this motor since the star segment is a small portion of the total grain (i.e. initial star grain length of 95 inches and an initial c.p. length of 613 inches). For motors with a star segment that comprises a larger portion of the total grain, however, the performance predictions with propellant deformations would be more greatly affected. The possibility of including star segments in future work in this area is discussed briefly in the Conclusion section of this thesis.

V. CONCLUSIONS

It has been shown that the strain analysis of this thesis has applications in the performance predictions of rocket motors. Additional comparisons are needed to substantiate the accuracy and usefulness of this technique, however, it is clear that the theory can be helpful in future SRM design and modification work. Such comparisons should include several different motors with different grain configurations. These grains should include variations on the straight c.p. grain such as slots or tapers as well as entirely different geometries such as star and wagon wheel grains. In the case of the star or wagon wheel grains, this analysis will have to be modified to predict the propellant deformation. One possibility would be to compute an effective bore perimeter for these more complicated grains, or perhaps an entirely different approach will be necessary.

More comparisons on the straight c.p. grains are desirable in order to verify that the performance prediction results shown for the two motors examined in this paper are typical for the general class of c.p. grain motors.

Future work in this area of propellant deformation should also examine the effect of changing the constraints and assumptions used in this analysis. For example, the uniform end loading assumed on the grain might better be approximated by the average of the internal pressure (P_1) and the axial propellant stress at the propellant-case inter-

face. Another possibility would be to use a non-zero value for the axial motor case stress. Some nominal value between zero and one half of the hoop stress may be chosen, or a value may be assumed based on the characteristics of a particular motor (i.e. thrust to weight ratio or case properties).

It is important to remember that one of the prime features of this analysis rests in the simplicity of its application in performance prediction programs. That is, the tangential strain relations are independent of axial position and are easily applied at any bore diameter. An increase in accuracy may be obtained be using a non-uniform end loading or a position dependent axial case stress, but this would entail more complex calculations to obtain the tangential bore strain.

In addition to improving motor performance predictions, the propellant deformation effects may also be useful in the examination of other SRM ballistic problems. The use of burning rate scale factors may actually disguise some ballistic effects. For example, from Figure 13, one can see that the areas under the performance prediction curves and the experimental data curve are not the same. This suggests a nozzle erosion rate discrepancy that would be hidden if the performance traces were matched by the use of a scale factor[5]. A refinement of the current propellant deformation theory and/or the strain analysis may lead the way in analyzing and correcting other performance prediction errors.

BIBLIOGRAPHY

1. Glick, R.L., Caveny, L.H. and Thurman, J.L., "Internal Ballistics of Slotted-Tube Solid-Propellant Rocket Motors," J. of Spacecraft and Rockets, April, 1967, pp. 525-530.

2. Barrere, M., Jaumotte, A., De Veubeke, B.F. and Vandenkerckhove, J., Rocket Propulsion, Elsevier Publishing Company, New York, 1960, pp. 277-281.

3. Timoshenko, S., Strength of Materials, D. Van Nostrand Company, Inc., New York, 1952, Part II, pp. 236-241.

4. Brisbane, J.J., "Heat Conduction and Stress Analysis of Solid-Propellant Rocket Motor Nozzles," Technical Report S-198, U.S. Army Missile Command, Redstone Arsenal, Alabama, 1969.

5. Sforzini, R.H. and Foster, W.A., Jr., "Solid-Propellant Rocket Motor Internal Ballistics Performance Variation Analyses (Phase Two)," Final Report, prepared for George C. Marshall Space Flight Center, NASA, Engineering Experiment Station, Auburn University, Auburn, Alabama, September, 1976.

6. Sforzini, R.H., "Analysis of Solid-Propellant Rocket Motors Using a Simplified Computer Program," Bulletin Fifty-Nine, Engineering Experiment Station, Auburn University, Auburn, Alabama, December, 1973.

7. "Technical Description of the TX354-5 Rocket Motor," Huntsville Division, Thiokol Chemical Corporation, Control No. U-67-1005A, May 9, 1967.